CEAS Space Journal (2023) 15:213–235
https://doi.org/10.1007/s12567-022-00429-0

ORIGINAL PAPER

Demisability assessment of space materials

B. Bonvoisin[1] · M. Meisnar[2] · J. Merrifield[3] · J. Beck[4] · T. Lips[5] · A. Guelhan[6] · T. Schleutker[6] · G. Herdrich[7] · A. Pagan[7] · E. Kaschnitz[8] · V. Liedtke[9] · B. Helber[10] · S. Lopes[10] · J. B. Gouriet[10] · O. Chazot[10] · T. Ghidini[1]

Received: 18 August 2021 / Revised: 7 January 2022 / Accepted: 31 January 2022 / Published online: 2 May 2022
© CEAS 2022

Abstract
Since March 2014, all ESA satellites and launcher upper stages which will be disposed of by atmospheric re-entry at the end of their operational life must demonstrate that the risk from fragments surviving the re-entry and causing casualties on ground is less than 1 in 10,000. This casualty risk is calculated by re-entry tools simulating the uncontrolled re-entry event using a computer aided design model of the spacecraft. The uncertainties on several parameters such as the aerothermodynamics fluxes model, the structural interfaces model, the materials model, and the level of detail of the spacecraft architecture will have an impact on the re-entry event simulation and the associated casualty risk calculations. To better understand the uncertainties associated to material modelling, five materials often used on space missions were tested in Plasma Wind Tunnels, mimicking atmospheric re-entry environment. Thermo-physical properties, thermo-optical properties and mechanical properties at high temperature were also characterized. Analysis of the samples after plasma wind tunnel tests was performed. A database compiling the materials properties measured and the plasma wind tunnel test results was created. The material properties characterised and generated during the activities will serve as inputs for the re-entry simulation events at equipment and system level.

Keywords Demisability · Design for demise · Plasma wind tunnel

1 Introduction

This paper presents the work and outcome of two studies initiated by the European Space Agency (ESA) on the demisability of space-relevant materials. Demisability test procedures were developed according to which five baseline materials were tested under representative conditions in the frame of the two projects CHARDEM and CoDM. Thermo-physical properties of the five materials were tested in the CHARDEM project, while emissivity and mechanical properties considering temperature were characterised in the CoDM project. Three plasma wind tunnel test campaigns were performed in parallel to determine the demise behaviour during atmospheric re-entry of the five materials of interest. The data generated during the two projects shall be used to reduce the uncertainties associated to material

✉ B. Bonvoisin
benoit.bonvoisin@esa.int

1 European Space Agency, Noordwijk 2201 AZ, The Netherlands

2 European Space Agency, ESA-RAL Advanced Manufacturing Laboratory, Harwell-Oxford Campus, Fermi Avenue, Didcot OX11 0FD, UK

3 Fluid Gravity Engineering Ltd, 1 West St, Emsworth PO10 7DX, UK

4 Belstead Research Limited, 387 Sandyhurst Lane, Ashford TN25 4PF, UK

5 HTG-Hyperschall Technologie Göttingen GmbH, Am Handweisergraben 13, 37120 Bovenden, Germany

6 Supersonic and Hypersonic Technologies Department, DLR-Deutsches Zentrum für Luft- und Raumfahrt e.V. (German Aerospace Center), Linder Hoehe, 51147 Cologne, Germany

7 IRS-Institut für Raumfahrtsysteme (Institute of Space Systems), University of Stuttgart, Pfaffenwaldring 29, 70569 Stuttgart, Germany

8 ÖGI-Österreichisches Gießerei-Institut, Parkstraße 21, 8700 Leoben, Austria

9 Aerospace and Advanced Composites GmbH, Viktor Kaplan-Straße 2, 2700 Wiener Neustadt, Austria

10 Aeronautics and Aerospace Department, Von Karman Institute for Fluid Dynamics, Waterloosesteenweg 72, 1640 Sint-Genesius-Rode, Belgium

modelling by the re-entry software. The resulting data was compared to the simulation models and used to set up a database for re-entry simulations. The demise is the result of an ablation process acting on an element (e.g. spacecraft, launch vehicle orbital stage, equipment, tank, reaction wheel) during a re-entry event to the extent that the resulting fragments no longer pose a casualty risk. The notion of demise or demisability can be applied at three different levels, spacecraft, equipment and material. The data generated during the above mentioned activities is focused on the demise at material level but can also be used as input for re-entry event simulations at system and spacecraft level.

2 Background

Since the beginning of space exploration, thousands of satellites have been launched into low earth orbit and only a fraction of these are still functioning. The remaining ones, or their fragments, can pose high risks to other satellites in orbit [1, 2] or to humans on Earth [3]. To mitigate the risks from space debris and ensure the sustainable use of our orbits, novel thinking with respect to spacecraft design and material selection is required. One option is de-orbiting through controlled re-entry protocols, which can be expensive. The other alternative is the un-controlled re-entry. This can lead to space debris impacting the Earth ground, posing risk for human safety. The current baseline is that the on-ground casualty risk shall not exceed 10^{-4} per spacecraft. With this in mind, the design-for-demise (D4D) initiative was introduced [4]. The idea is to design spacecraft such that the entire or the majority of the spacecraft disintegrates upon re-entry into the Earth's atmosphere [5–7].

The most critical parameter for the demise behaviour of a spacecraft is the break-up altitude, at which critical components are released and exposed to the entry flight environment. The most important factors for the demisability of a component (e.g. tank, magnetic torquer, reaction wheel) are its geometry, its position within the spacecraft and the materials it is made from.

Material selection must include considerations with respect to the part's functionalities and the requirements of the mission profile. Conventionally, during the materials selection process, properties such as tensile strength, hardness, fracture toughness, electrical and thermal properties and many others are considered. Only recently, demisability has become a factor that is being considered during material selection of a spacecraft component.

However, very little information exists on the behaviour of materials exposed to the conditions occurring during re-entry flight. It is believed that spacecraft propellant tanks made of titanium alloys or carbon fibre reinforced polymers (CFRPs) pose the highest on-ground risk due to their low demisability and their very frequent use. Reports of a CFRP tank from the Atlas Centaur upper stage that survived atmospheric re-entry and was found on ground in Spain demonstrate the importance of the D4D concept [8]. Recent progress was made in the ongoing development of the Spacecraft Atmospheric Re-entry and Break-Up (SCARAB) [9] and Object Reentry Survival Analysis Tool (ORSAT) software tools [10]. These software packages were built to analyse the thermal and structural effects of atmospheric re-entry of spacecraft with a finite-element approach [11, 12]. However, it was found that simulations of more complex structures and exotic materials such as CFRPs are very difficult [8] and more experimental data and improved numerical models are required for reliable predictions.

Table 1 Chemical composition of AA7075 used in the CHARDEM study

Element	Si	Fe	Cu	Mn	Mg	Cr	Ni	Zn	Ti	Zr	Al
wt%	0.06	0.17	1.51	0.07	2.34	0.19	< 0.01	5.8	0.02	< 0.01	Bal
Min	–	–	1.2	–	2.1	0.18	–	5.1	–	–	–
Max	0.40	0.50	2.0	0.30	2.9	0.28	–	6.1	0.2	–	–

Table 2 Chemical composition of AISI 316 used in the CHARDEM study

Element	C	Si	Mn	P	S	Cr	Mo	Ni	N	Co	Fe
wt%	0.014	0.33	1.87	0.04	0.001	16.5	2.0	10.12	0.045	0.21	Bal
Min	–	–	–	–	–	16.0	2.0	10.0	–	–	–
Max	0.03	0.75	2.00	0.045	0.03	18.0	3.0	14.0	0.10	–	–

3 Materials tested

A number of materials commonly used for spaceflight were tested within the framework of this study and are introduced in the following sections. Please note that the chemical compositions were characterised by X-ray fluorescence for the materials used in the CHARDEM project. While the nominally same alloys have been used in CoDM, the material datasheets allow some variation in the chemical composition. This can have an impact on the material properties relevant for the demise process. The following tables provide the alloy specification (min and max element share) along with the composition measured in the CHARDEM project.

3.1 Aluminium alloy 7075-T7351

This material is a typical aluminium alloy with high strength and fatigue resistance. It is one of the alloys most often used for building rocket and satellite parts (Table 1).

3.2 Stainless steel AISI 316L

The stainless steel AISI 316L is a highly alloyed austenitic grade and one of the steels that is most widely used in the space industry. It is hardenable by cold forming and offers a high corrosion resistance in acids, chlorides and at elevated temperatures (Table 2).

3.3 Ti-6Al-4V

The titanium alloy Ti6Al4V, also known as Grade 5, is the most commonly used alloy of titanium. It is a heat-treatable alpha–beta-alloy with an excellent combination of strength, corrosion-resistance, weldability and processability (Table 3).

In addition, additively manufactured (AM) Ti-6Al-4 V, prepared by SLM, was tested as well (in the CHARDEM project) in order to identify whether differences between the demise behaviour of conventional and AM Ti-6Al-4 V can be observed.

3.4 CFRP

The CFRP characterised in the CHARDEM study was made from unidirectional prepregs with article code CM-Preg-T-C-2 450/635 from supplier CMP. It consists of XN-60-60S fibers from Nippon Graphite Corporation and an epoxy resin CP0031. Neither the fiber nor the resin are space qualified. However, the fibre (tensile modulus 620 GPa, fiber diameter 10 µm) is a good representative for high modulus carbon fibers, which are commonly used in space industry. The thermosetting matrix material being an epoxy resin is also quite common.

There were three layers of unidirectional carbon fibre per millimetre. The fibres were non-woven and the orientation of the fibres was altered with each layer. The fibre volume fraction was, according to the manufacturer, approximately 64%.

In the CoDM study, a CFRP composite composed of an EX-1515 cyanate ester resin and Torayca M55J carbon fibres was investigated.

3.5 SiC

SSiC is used for optical payloads and ultra-stable structures for space applications thanks to its high specific thickness and thermal dimensional stability. The sintered silicon carbides (SSiC) tested were manufactured by Boostec (CHARDEM) and by H. C. Starck GmbH (CoDM). The Boostec® SiC is a polycrystalline ceramic of ultra-pure alpha SiC type, obtained by pressure-less sintering of a mixture of mainly 6H and 4H polytypes.

The SSiC manufactured by H. C. Starck GmbH is also obtained by pressure-less sintering.

4 Methodology

The characterisation methodology for the assessment of the behaviour of a material with regards to demisability is summarised in Fig. 1 and further described in Sects. 4.1–4.4. It begins with the measurement of the thermo-physical, thermo-mechanical and thermo-optical properties of the material under investigation, followed by plasma wind tunnel (PWT) tests to simulate realistic atmospheric re-entry conditions. This is followed by post-test characterisation of the samples exposed to the wind tunnel tests. In parallel, the thermo-physical properties are used as a basis for numerical simulations, modelling the material in the wind tunnel experiments and their degradation. Finally, the simulated and experimental results are compared.

4.1 Thermo-physical properties

The measurements of the thermo-physical properties were conducted by ÖGI (Österreichisches Gießerei-Institut). The thermal conductivity, the specific heat capacity, heat of solid-state phase transitions and heat of fusion, the density and the thermal expansion were measured as functions of the temperature. The specific heat was measured via differential scanning calorimetry (DSC) using a NETZSCH DSC 404 Pegasus. A different technique was used for measuring the mass loss with temperature—the differential thermal analysis with thermo-gravimetry (DTA/TG) was conducted using

a NETZSCH STA 449F3 Jupiter for the measurements. The pulse heating calorimeter that was used for measurements at high temperatures was developed and built by ÖGI. The thermal expansion was measured with a double-pushrod dilatometer NETZSCH DIL 402.

4.2 Mechanical properties

Mechanical properties under thermal loads by one side irradiation were measured in AAC´s Re-Entry Test Chamber. The test set-up consisted of a sample holder based on cold grippings, and a graphite susceptor tube irradiating the tensile-loaded specimens from one side. Sample backside temperature was recorded by a two-colour pyrometer.

4.3 Emissivity measurements

The emissivity measurement facility (EMF) of IRS has been qualified for the measurement of total and spectral emissivities for a wide range of materials. A heated graphite tube is used for generating the equivalent black body cavity (apparent emissivity > 0.999). The sample is initially positioned in a sample holder mounted on a piston at one end of the tube and indirectly heated until near-isothermal conditions are achieved. The pyrometrically obtained temperature, as measured through an optical window at the far end of the tube, corresponds to the approximate black body temperature of the surface. By rapidly shifting the piston to a forward position outside of the heated tube closer to the window, the sample is removed from its previous black body context, which allows for an extraction of emissivities based on both of the measured apparent temperatures. Both wavelength-selective and -nonselective devices can be deployed to obtain spectral and total emissivity measurements. An argon atmosphere is provided to inhibit damage to the tube at temperatures above 1800 K. For total emissivity measurements, a pyrometer with a sensible wavelength interval of 0.4–8 µm is generally used, which, at a temperature of 2073 K, can capture 97.75% of Planck's distribution. The full compatibility of the EMF's sample holder with the coin-type sample geometry utilized in the CoDM test campaigns allows for a characterization of surface emissivities for material samples both in their pristine and post-test states [13].

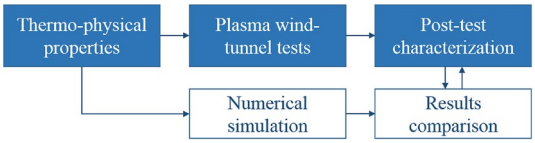

Fig. 1 Demisability test procedure

4.4 Plasma wind tunnel testing

All materials were tested for their demise behaviour when being exposed to realistic re-entry conditions via plasma wind tunnel testing [14]. In the frame of the CHARDEM project, the testing was performed by the German Aerospace Centre (DLR) using their L2K (low heat flux) and L3K (high heat flux) wind tunnel facilities. In the CoDM study, the experimental re-entry simulation was conducted by Institute of Space Systems (from German: Institut für Raumfahrtsysteme—IRS) at the University of Stuttgart using their PWK1 and PWK4 plasma wind tunnel facilities, as well as in the Plasmatron test facility at the von Karman Institute for Fluid Dynamics (VKI). An overview of the facility envelopes is given in Table 4

The L2K wind tunnel uses a Huels-type arc heater with a maximum electrical power of 1.4 MW to energise the working gas to high enthalpy conditions. This allows achieving cold wall heat fluxes of up to 3.0 MW/m^2 at stagnation point pressures of up to 250 hPa. Hypersonic free stream velocities are provided by a convergent-divergent nozzle. The nozzle's expansion part is conical with a half angle of 12°. Different throat diameters of 14 mm, 20 mm, 25 mm and 29 mm are available and can be combined with nozzle exit diameters of 50 mm, 100 mm and 200 mm, and 300 mm. Consequently, the facility setup can effectively be adapted to particular necessities of a certain test campaign.

The L3K wind tunnel uses a segmented type arc heater with a maximum electrical power of 6 MW. This allows cold wall heat flux rates of up to 16 MW/m^2 at stagnation pressures up to 2000 hPa. Combinations of the same throats and nozzles as for the L2K provide Mach numbers between 3 and 10 at Reynolds numbers up to 10,000/m. Both the L2K and the L3K facilities were operated with air for the CHARDEM tests.

The CHARDEM samples were cylinders and cuboids with a diameter / side length of 50 mm and a thickness of 20 mm. The rotational symmetry of the cylindrical samples

Table 3 Chemical composition of the Ti-6Al-4V alloy used in the CHARDEM study

Element	Al	V	Fe	Y	O	C	N	residual	Ti
wt%	6.23	3.98	0.19	< 0.001	0.198	0.004	0.004	0.4	Bal
Min	5.5	3.5	–	–	–	–	–	–	–
Max	6.5	4.5	0.25	–	0.20	0.08	0.03	0.4	–

simplifies the interpretation of the test results and the numerical rebuilding. The cuboid samples were meant to reveal potential impact of the shape and the edge effects. The high thickness was chosen to allow the samples to reach steady-state demise, which is of high interest for fitting of the numerical models, and for getting measurable temperature difference over the samples thickness even for highly conductive materials. The samples were screwed onto the sample holder with ceramic paper insulation in between the two.

The instrumentation concentrated on the observation of the material behaviour and the evolution and distribution of the temperatures. Accordingly, cameras were used for observing the samples in the visible and infrared range. The temperatures derived from the infrared video data were compared to those recorded with spectral and two-colour pyrometers and integrated thermocouples. The emissivity depends not only on the temperature and spectral range, but also on the evolution of the surface (duration of exposure, chemical environment etc.). Accordingly, the emissivity changes during the test and the optical temperature measurements have high uncertainties. The approach of the CHARDEM project was to implement thermocouples within the samples. This intrusive measurement does not require knowledge of material properties. The reader is invited to compare with the different solution used in the CoDM project described below.

The IRS plasma wind tunnel facility PWK1 [15] employs the Self-Field Magnetoplasmadynamic Generator (SF-MPD) RD5, designed to generate high-enthalpy, low-pressure air flows. These conditions allow to emulate stagnation point heating with dissociation degrees relevant e.g. to hyperbolic entry conditions or the early/pre-break up phase of an uncontrolled atmospheric entry from LEO.

The PWK4 facility [15] utilizes a thermal arc heater, capable of generating super- to hypersonic air plasma flows at pressure and enthalpy levels relevant to those experienced e.g. by debris objects following spacecraft break-up. Both the RD5 and RB3 plasma generator designs feature a hot concentric tungsten cathode design, resulting in minimal impurities in the plume.

For the CoDM test campaign, coin-type conical flat disk material samples with thicknesses ranging between 3 and 4 mm were deployed, using 50 mm diameter flathead probes with radiatively cooled SiC caps. Radial and structural heat losses were minimized through effective thermal insulation, with the samples further being mechanically constrained and shielded from the flow at their respective edges. This had the effect of emulating both an enclosed structural context as well as quasi-1D heat conduction conditions, which suppressed unwarranted delamination of laminate materials and simplified the post-test analysis.

Front and back surface temperatures were both monitored using single-colour and narrowband pyrometric devices and a thermographic imaging camera, with temperature-dependent emissivities as determined using the EMF applied for a correction of the measured front surface temperatures. The surface phenomenology of samples was monitored using HD video cameras. Characteristic atomic and diatomic species emanating into the boundary layer were identified through optical emission spectroscopic measurements within a control volume of approximately 3 mm diameter before the stagnation point of the exposed samples. The pre- and post-test states of the samples were further documented through a measurement of their physical properties and optical microscopy.

For the primary PWT test campaign at IRS, material samples were subjected to plasma exposure indefinitely, with the respective test being terminated by shutdown of the plasma generator either when the sample demised or had attained thermal equilibrium. Different heating conditions were characterized and applied to assess the effects of varying heat fluxes. An additional series of steady-state thermal response tests was conducted for the high-temperature materials SSiC, AISI 316L and Ti6Al4V in order to provide data conducive to the calibration of models representing the effects of catalytic recombination.

The VKI Plasmatron is equipped with a 160 mm diameter Inductively Coupled Plasma (ICP) torch powered by a high-frequency, high-power, high-voltage (400 kHz, 1.2 MW, 2 kV) generator. The gas is heated by induction through a coil, providing a high-purity plasma flow. The 160 mm diameter plasma torch provides a plasma jet in a 2.5 m long, 1.4 m diameter test chamber, kept below atmospheric pressure. The plasma jet size and the testing chamber allow a broad range of test article dimensions. Heat fluxes from ~ 90 kW/m^2 up to and exceeding 10 MW/m^2 guarantee enthalpies between ~ 5 and ~ 65 MJ/kg. Pressure can range between 2 and 400 hPa [16].

The test sample geometry selected for this project was a flat face geometry with a diameter of 50 mm and a corner radius of 11.75 mm (very similar to the IRS variant). This geometry is suitable to promote typical non-equilibrium boundary layer. It is the baseline shape for catalycity and emissivity testing and has been designed for truncated conical samples with variable thickness (usually between 1 and 3 mm) and an external diameter of 26.6 mm. A cover made of graphite (Grade GR008G, Graphtek LLC) or silicon carbide (StarCeram®S SSiC, H.C. Starck) was attached to the water-cooled holder by three metallic pins supporting the sample. A thick cork insulation layer was placed as back support of the samples to limit the heat flux dispersion by conduction. During the research project, different materials have been evaluated for this insulation layer placed on the back of the sample: virgin and aged cork composite (P50, Amorin Cork Composite) and virgin ceramic composite (Procelit 180, Morgan Thermal Ceramics). An intensive

Table 4 Known stagnation point condition envelopes for air flows of PWT facilities deployed in CHARDEM and CoDM as well as sample types, mounts and diagnostic tools deployed in respective test campaigns

Facility	L2K (DLR)	L3K (DLR)	PWK1 (IRS)	PWK4 (IRS)	Plasmatron (VKI)
Plasma Source	Huels-type arc heater	Segmented-type arc heater	Self-field magneto-plasma-dynamic generator (SF-MPD) RD5	Thermal arc plasma generator with concentric cathode (TPG) RB3	Inductively-coupled plasma generator
Stagnation pressure/hPa	< 250	< 2000	< 50	< 500	< 400
Mass-specific enthalpy (air) / MJ/kg	3–15	6–20	12–220	0.5–30	5–65
Cold wall heat flux (typical)/MW/m^2	< 3.0	< 16	0.13–15	0.25–5.0	0.1–5 (above 5: supersonic)
Mach number	3–6	3–10	< 2.3	< 5.3	< 0.3 (typical operation)
Nozzle exit diameter/mm	50–200	50–300	180	88	160 (no nozzle)
Sample type	Cubes and cylinders with side length/diameter of 50 mm and thickness of 20 mm		26.5 mm diameter truncated flat cone (3–4 mm thickness)		26.5 mm diameter truncated flat cone (3.57 mm thickness)
Sample mount	Samples held in position via three screws on their back. Copper holder, thermally decoupled from the sample via ceramic paper		50 mm diameter "flat head" geometry with radiation-cooled SiC cap		50 mm diameter "flat head" geometry with radiation-cooled graphite or SiC cap
Diagnostics	Front surface temperatures via single-colour pyrometry, two-colour pyrometry and infrared thermography Demise behaviour observation via SD video kameras Measurement of internal temperatures via integrated thermocouples FTIR for analysis of the pyrolysis gases composition		Front surface temperature via single-colour pyrometry and infrared thermography Back surface temperature via narrowband pyrometry HD video, optical emission spectroscopy in boundary layer		Back surface temperature Back insulation temperature 2-colour pyrometry HD video, optical emission spectroscopy

thermal analysis of the complete sample holding system has recently been carried out and supports the experimental analysis during ongoing and future material tests [17].

The test assembly (sample, insulation and cover) was instrumented with several type-K thermocouples to measure the back temperature at different positions during the plasma exposure. A two-color pyrometer (Marathon Series MR1SB Raytek Corp., Santa Cruz, CA) was used to obtain the emissivity independent surface temperature on the sample at a given location. A blackbody reference source (LANDCAL R1500T, LAND Instruments International) has been used to calibrate the two-color pyrometer. The boundary layer in the neighborhood of the stagnation point was observed by a low resolution optical emission spectrometer (Ocean Optics HR4000CG-UV-NIR). The detection of the time evolution of the species just above the material surface allow to correlate the boundary layer information with the surface data obtained from the other measurement techniques. Two video cameras complete the optical devices installed on the Plasmatron. Through they are off-the-shelf non-scientific instruments, they have revealed to provide interesting insight on the behavior of the material exposed.

4.5 Microstructural analysis

Microstructural analysis was performed by both ÖGI and the ESA-RAL Advanced Manufacturing Laboratory (AML) for determining the impact of the PWT tests on materials. The microstructure results obtained after PWT testing could be directly compared with microstructures found on fragments post re-entry. Hardness testing, optical microscopy, SEM and laser Raman microprobe were used. The hardness measurements were carried out according to standards EN ISO 6506-1 and 6507-1 using an Emco Test M5 U hardness tester at ÖGI and with a Struers Durascan G5 at AML. Macroscopic pictures were shot with a Nikon digital camera D90. The stereomicroscopic recordings were accomplished by a ZEISS microscope V12 Discovery with a digital camera DP50-Cu. For optical microscopy a BX51/BX60M with a motorized specimen table was used (ÖGI) as well as an Olympus DSX500 (AML). A FEI Quanta 200 Mk2 SEM with an INCA Energy 200 Oxford EDX-Device (ÖGI) and a Zeiss LEO 1530 VP SEM fitted with an Oxford Instruments Xmax80 SDD detector (AM) were used for characterisation of the microstructure. Furthermore, a Jobin Yvon LABRAM confocal-Raman spectrometer equipped with a frequency

doubled Nd-YAG laser (100 mW, 532.2 nm) and with a He–Ne laser (633 nm), and diffraction gratings of 1200 and 1800 grooves/mm was used to measure the oxide layer of the Ti-6Al-4 V samples. Detection was done with a Peltier-cooled, slow-scan, CCD matrix-detector. Laser focussing and sample viewing were performed through an Olympus BX 40 microscope fitted with 10 ×, 50 × and 100 × long-working distance objective lenses (allowing viewing in reflected- and transmitted-light).

For the analysis of the carbon fibres at the front sides of the damaged samples, ÖGI used a device from Zeiss, Type EVO MA 10. The FTIR Analysis was performed using a Spectrometer of the type Perkin-Elmer, Modell Spectrum One.

4.6 Numerical simulation

Software can be used to perform re-entry simulation at equipment, systems and spacecraft level. Software can also be used for rebuilding plasma wind tunnel tests and to derive material properties based on the heat profiles measured during the PWT tests. The software tools used for uncontrolled re-entry events simulations use the thermo-physical properties characterised during the activities for decreasing the uncertainty associated with material modelling. Emissivity is an important parameter as it evolves in function of the temperature, time and the atmosphere surrounding the surfaces of interest; especially for metallic materials. The emissivity values used by the tools utilized in the presented studies were updated based on the work performed in this paper. The tool used for the numerical simulations of the CHARDEM study was the SCARAB code (Spacecraft Atmospheric Re-Entry and Aerothermal Break-Up) [9–12] with version 3.0. The so-called wind tunnel mode of SCARAB, that had already been implemented for numerical rebuilding of wind tunnel tests, was used. SCARAB allows the analysis of mechanical and thermal destruction of controlled or uncontrolled spacecraft and other objects during re-entry. It is an integrated software package (flight dynamics, aerodynamics, aero thermo-dynamics, thermal- and structural analysis) used to perform re-entry risk assessments (quantify, characterize and monitor surviving fragments during re-entry). The software application has been validated with in-flight measurements and re-entry observations, and it has been compared to other re-entry prediction tools of the international community. SCARAB has been developed under ESA/ESOC contracts since 1995 under the lead of Hypershall Technologie Göttingen GmbH (HTG) and with support from other European and international partners. It is considered operational software. The software development has evolved over time, based on lessons learned from preceding software versions, upgrades and specific requests on re-entry analyses performed for numerous European satellites and launcher stages.

Please regard that SCARAB has been extended and improved since the CHARDEM study. The current version, SCARAB 4.0, includes new modelling approaches that would yield different results, if the simulation were repeated. For example, a more realistic heat flux mapping is used.

In the CoDM study, the SAMj destructive re-entry code, a collaborative development between Fluid Gravity Engineering and Belstead Research, has been used. SAMj has been used in a number of ESA activities, inclusive of system level analysis and wind tunnel test rebuilding. SAMj pioneered the concept of a component-based demise tool where a set of primitive components are connected using joints to construct a complete spacecraft. The ESA DRAMA tool has recently adopted this approach. SAMj contains a number of unique demise models, inclusive of a specific model for the demise of glass materials by shear, and the inclusion of a catalycity model, which was developed for the CoDM activity.

This integrated toolset comprises eight modules, which may be used individually or in combination as shown in Fig. 2.

- *RCR* re-entry casualty risk analysis. RCR combines the ATS6, ATS3, AHM, VFM and DCS modules to provide an integrated, fast, accurate, state-of-the-art probabilistic engineering assessment of the on-ground casualty risk from a destructive re-entry. It is ideally suited to early stage vehicle design analysis.
- *ATS3* high performance 3 degree of freedom atmospheric trajectory code. ATS3 projects ballistic trajectories through layered atmosphere models. It delivers a high degree of extensibility through its modular architecture and scripted configuration. ATS3 supports the use of a range of customisable planet, gravity and atmosphere models.
- *ATS6* 6 degree of freedom atmospheric trajectory code. ATS6 projects trajectories through atmosphere models, generating vehicle attitude information in addition to position and velocity. Like ATS3, it delivers extensibility through modularity and scripted configuration.
- *AHM* atmospheric re-entry aerothermal heating module. When linked with ATS3 or ATS6, AHM calculates the aerothermodynamic heating on a vehicle or fragment throughout its entry trajectory, and provides an assessment of the temperature history and ablation. AHM uses a novel application of the Heat Balance Integral (HBI) method by default, but alternatively a full 1D ablation model can be embedded.
- *CAM* conduction ablation model. CAM is a one-dimensional heat conduction model which accounts for ablation due to pyrolysis and surface chemistry. CAM can be used

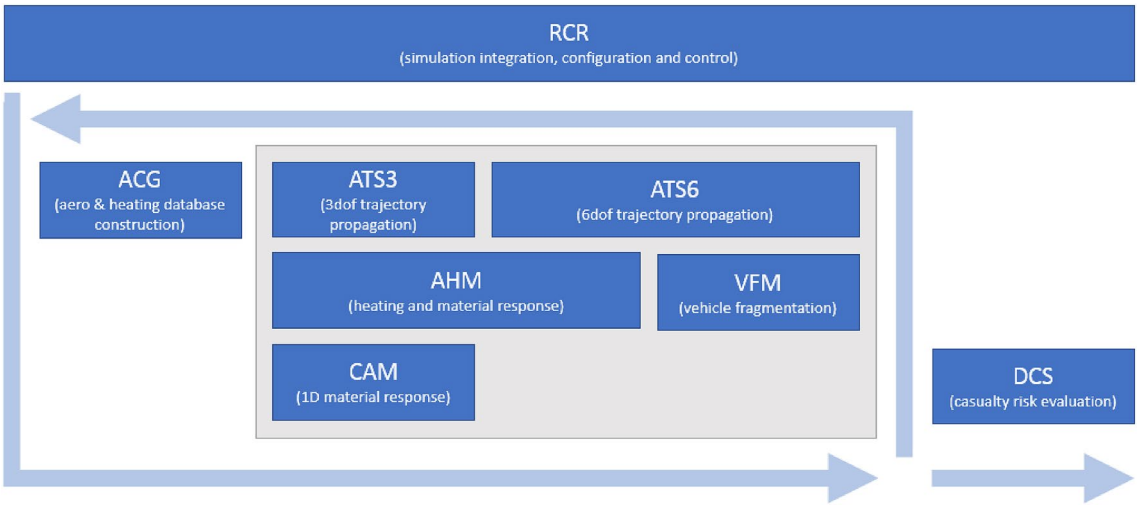

Fig. 2 SAM destructive re-entry framework

as a standalone design tool for heatshield sizing, or can be embedded within AHM.

- *ACG* 6 degree of freedom vehicle drag and heating coefficient evaluation code. ACG is implemented using either a ray-traced, or simple panel, method to generate shaded or unshaded drag and heating coefficients. ACG supports the evaluation of complex vehicle geometries composed of geometric primitives linked by joints. It also contains a number of state-of the-art correlations for primitive shapes which account for flow properties such as stream-length, and a unique mechanism for combining these correlations into heating profiles for compound shapes.
- *VFM* vehicle fragmentation assessment. When linked with ATS6, VFM evaluates the break-up of complex geometries, based on aerodynamic and heat loading. The fragmentation criteria used are based on available experimental data, rather than simple modelling assumptions.
- *DCS* space debris casualty simulation. DCS converts a series of fragment impact points into a probability track on the earth's surface; and assesses the associated probability of human casualties against third party population density maps.

5 Test results

5.1 Thermo-physical properties

The specific heat capacity and enthalpy, thermal expansion, density and thermal conductivity were measured as a function of the temperature in the CHARDEM study. The following results accordingly refer to the respective materials, but are expected to be representative also for the similar alloys used in CoDM. This does not apply to the CFRP. The measured thermo-physical properties (e.g. density, specific heat capacity and enthalpy, thermal expansion, density and thermal conductivity) are directly used by the re-entry software for metallic materials, while equivalent properties can be derived from plasma wind tunnel test rebuild for more complex materials modelling (e.g. CFRP).

For the metallic samples, the results were very much aligned with the literature data and no deviations from the expected values were discovered. The specific heat of the aluminium alloy and stainless steel samples increased approximately linearly with the temperature, while the profile of the Ti-6Al-4V showed the characteristic alpha-to-beta transition at ~ 950 °C. For all three alloys, positive volume expansion was observed in a linear fashion. The thermal conductivity also increased linearly with growing temperature for Ti-6Al-4V and stainless steel, whereas it remained fairly constant for AA7075 at around 165 W/m/K up to 550 °C.

For the samples of the CFRP made from XN-60-60S, a significant mass loss of 20% was recorded between 320 and 400 °C during the DTA/TG measurements (Fig. 3a). The CFRP material could only be tested until onset of the thermal decomposition. The reaction heat absorbed by the decaying process became apparent in the DSC measurements (Fig. 3b). As the partial pressure of oxygen is very low in the hot phase of the entry flight, the oxidation of matrix is very limited. Reflecting this, all thermophysical characterization tests were conducted in pure Argon atmosphere. The observed mass loss is accordingly caused by the endothermic decomposition, that produces smaller, gaseous molecules and leaves behind the graphite fibres as flakes. For that reason, the charred specimens could not be measured, as the graphite flakes had insufficient mechanical stability.

The amount of char formed during the thermal decomposition of the matrix depends on the matrix material, curing conditions, testing atmosphere, range of temperature increase etc. This residual char typically holds the fibres and in combination with them forms a solid carbon–carbon (C/C) composite. Decomposition down to dry fibres is the ideal case for demisability, but rarely observed. This is reflected in the collected test data presented later, that show a surprisingly high demisability. In the last years, many other composites have been tested and the XN-60-60S based composite discussed here, so far, was the only one with this beneficial behaviour.

The heat of the solid-state phase transformation in the CFRP is also shown in the apparent heat capacity plot (Fig. 4a). The specific heat capacity of the SiC sample as a function of temperature is shown in Fig. 4b. It follows a parabolic curve and solid-state transformation was not observed for this material. The thermal volume expansion of the SiC material was nearly linear with the temperature between 0 and 1500 °C, although the measurement uncertainty increased towards higher temperatures.

Of all the studied materials, the SSiC thermally expanded the least (1.020% up to 1500 °C). The materials' densities at room temperature (RT) are listed in Table 5. The densities at elevated temperature were calculated from the thermal volume expansion and were observed to decrease near-linearly with increasing temperature.

5.2 Mechanical properties characterized by AAC

In the screening stage, samples were exposed to constant heat fluxes, and resulting temperatures and samples survival times before mechanical failure had been investigated (Table 6).

Al2017 was tested instead of Al7075, which could not be procured with the thickness required for this specific test. The failure of Al2017 (low melting point) and Ti6V4Al (low thermal conductivity), and the survival of SiC are in line with expectations. SS316L showed substantial elongation after exposure to the highest heat flux, and the CFRP matrix was degraded in the centre of the samples, but the load could be transferred by the carbon fibres.

The selected profiles for final tests can be seen below. Heat fluxes and corresponding susceptor tube temperatures for various profiles for ARV are shown in Fig. 5: an overview of the mechanical test results is presented in Table 7.

Heat fluxes converted to blackbody heater temperatures are shown in Fig. 6:

5.3 Emissivity measurements

Using the emissivity measurement facility (EMF) at IRS, the temperature-dependent total and pyrometer-device specific emissivities of materials investigated in CoDM were measured both in their pristine and post-PWT-test states. For all of the investigated metal alloys and SiC, which are respectively subject to the formation of passive oxide layers in high-enthalpy oxidising plasma flows, it was found that this coincides with a dramatic increase of the total normal emissivity. This is generally considered detrimental to demise as it increases the material's ability to dissipate heat for high-temperature alloys in particular [18].

Selected emissivity measurement result data for aluminium alloy 7075 and type 316L stainless steel are given in Fig. 7. Whereas most measurements, specifically those determined for post-test sample and for SSiC and the investigated aluminium alloys in general, agree well with literature data and recent findings from third parties.

For CFRP EX-1515/M55J, it was tentatively concluded that the error introduced by the considerably accelerated cooling of charred CFRP even during the fast shift of the EMF's piston was too great for practical application of the measured values, which manifested itself in a drop of the emissivity over increasing black body temperatures. For the purpose of the CoDM activity, a constant emissivity of 0.85 was assumed, however, the methodology for measuring the emissivity of rapidly cooling materials with a low heat capacity has since been improved.

5.4 Plasma wind tunnel tests in the CHARDEM study

A comparison of the time versus temperature diagrams during wind tunnel testing between the aluminium alloy and stainless steel sample is given in Fig. 8.

Due to the high thermal conductivity of AA7075, the thermal gradient through the thickness of the sample is small. As a result, the entire sample softened and deformed very quickly upon reaching high enough temperature, however, without any material spillage. The maximum temperature recorded was 608 °C (Fig. 8a). This is well below the liquidus point of the alloy (635 °C). As the material has a wide temperature range between solidus point (477 °C) and liquidus point, the sample was likely in a state of low viscosity but not yet in fully molten, when deformation started. An oxide bag was formed around the sample.

The stainless steel showed a different demise behaviour than the aluminium alloy (Fig. 8b). This is due to the comparatively low thermal conductivity, that allows much higher temperature differences over the sample at the given heat flux rates, and the narrow temperature range between the solidus and the liquidus. This resulted in a slow melting

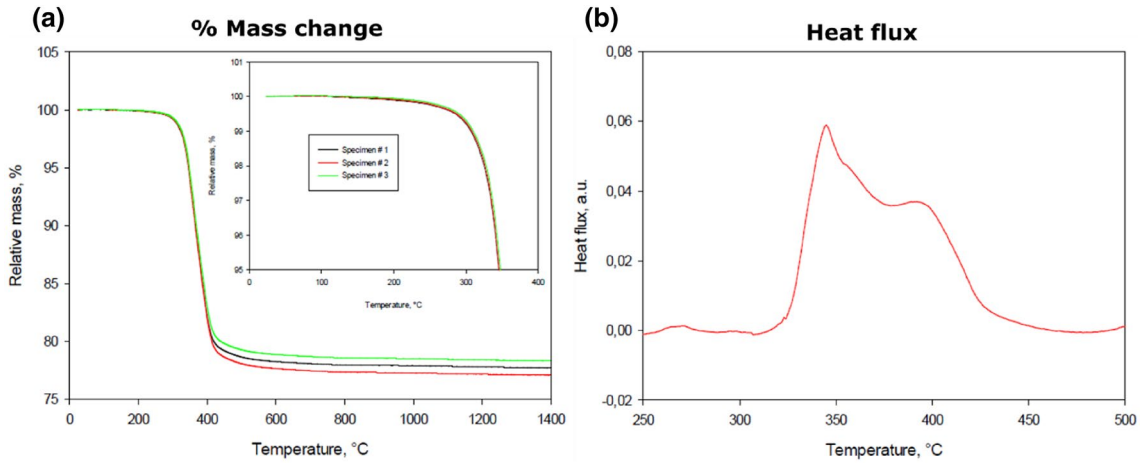

Fig. 3 Mass change and heat flux in CFRP upon heating from room temperature to 1400 °C

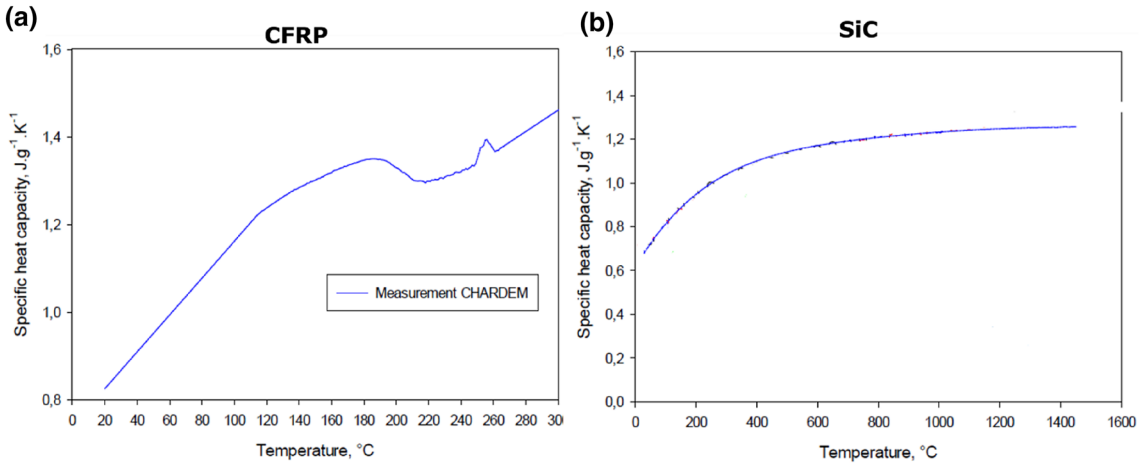

Fig. 4 Specific heat capacity of CFRP and SiC materials

of the surface with spilling of liquid steel while the sample body remained solid. As a result, the sample basically retained its shape despite demising for roughly 25 s.

At the low heat flux condition, the Ti-6Al-4V was not demised. The demise temperature of the titanium was not achieved at the 1.2 MW/m^2 cold wall heat flux. The samples quickly started to demise at the higher heat load of 2.3 MW/m^2. The titanium alloy was, in this case, heated to over 1000 °C within 20 s. Combined with the comparatively low thermal conductivity, a high temperature difference over the samples could be observed by the thermocouples. The maximum temperature observed in the test of 1755 °C was measured optically with the pyrometers. This temperature is above the melting point of the titanium alloy, but below the melting point of titanium dioxide (1843 °C) and titanium nitride (2930 °C). The post-test characterization will discuss this in more detail, but from the wind tunnel experiments, it appears likely that an insulating oxide layer formed at the front of the sample. This oxide layer leads to an overheating, that can be a result of the thermal resistance or the mechanical containment of the melt behind the layer and thus delays the demise of the sample.

Table 5 Density measurements at RT performed with Archimedean balance

	AA7075	AISI 316	Ti-6Al-4V	CFRP	SiC
Density at RT (kg/m^3)	2800	7950	4400	1720	3160

The optical temperature measurements of the XN-60-60S based CFRP samples (Fig. 9) revealed that the demise occurs by periodic layer-by-layer ablation. During each period the front layer of carbon fabric is exposed to the flow for some

Table 6 Back side temperatures and survival times for the tested materials

Material	Property	Heat Flux [kW/m^2]				
		300	400	500	700	950
Al2017	Backside Temp [°C]	515	586			
	Survival time [min]	06:20	00:10			
Ti6V4Al	Backside Temp [°C]	894	950	1204		
	Survival time [min]	0:30:00	16:40	06:50		
SS 316L	Backside Temp [°C]	841	906	978	1088	>1220
	Survival time [min]	0:30:00	0:30:00	0:30:00	0:30:00	04:20
CFRP	Backside Temp [°C]	712	758	801	865	927
	Survival time [min]	0:30:00	0:30:00	0:30:00	0:30:00	0:30:00
SiC	Backside Temp [°C]					>1220
	Survival time [min]					0:30:00

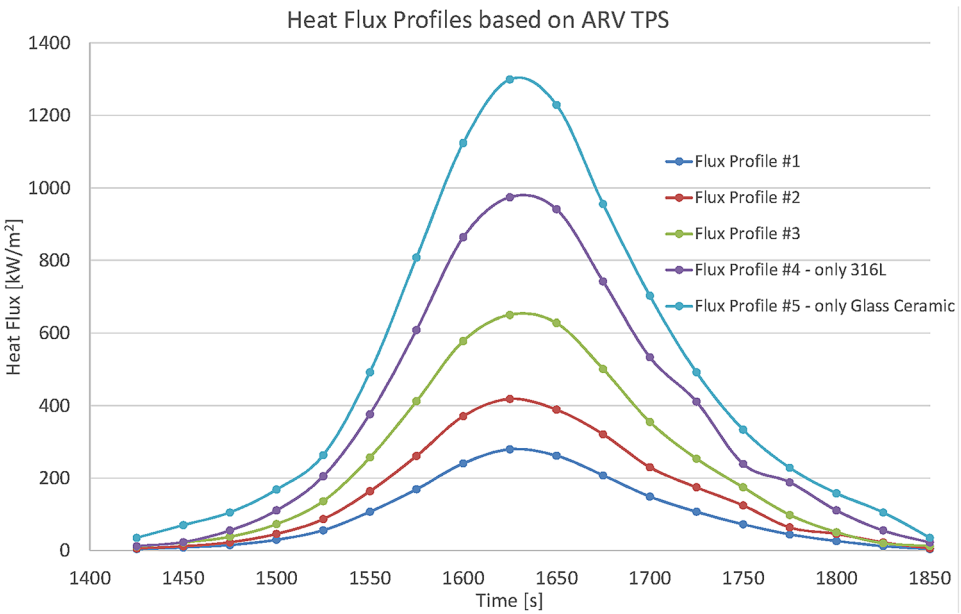

Fig. 5 Heat fluxes and corresponding susceptor tube temperatures for various profiles for ARV

Table 7 Overview of mechanical test results

Material	Max Temp Susceptor (°C)	Max Temp Backside (°C)	Peak Heat flux (kW/m^2)	Average load before failure (N)	Failure description
Glass ceramic	1216	882	279	0	No damage after test
Glass ceramic	1569	1081	651	0	No permanent elongation
316L	1443	827	492	949	None
316L	1570	947	651	50	None
316L	1762	1056	975	50	None

time. The measured surface temperature first increases very fast and then approaches an equilibrium temperature with a decreasing rate. Eventually, the front layer is blown off and the next layer is exposed to the flow and the periodic behaviour starts again.

In contrast, SiC is a material famous for high temperature application and a potential candidate for future non-ablative heat shields because of its very low demisability. The reason for this is the extremely high melting point, combined with a high thermal emissivity and oxidation resistance of the ceramic. Thus, there was no common demise behaviour

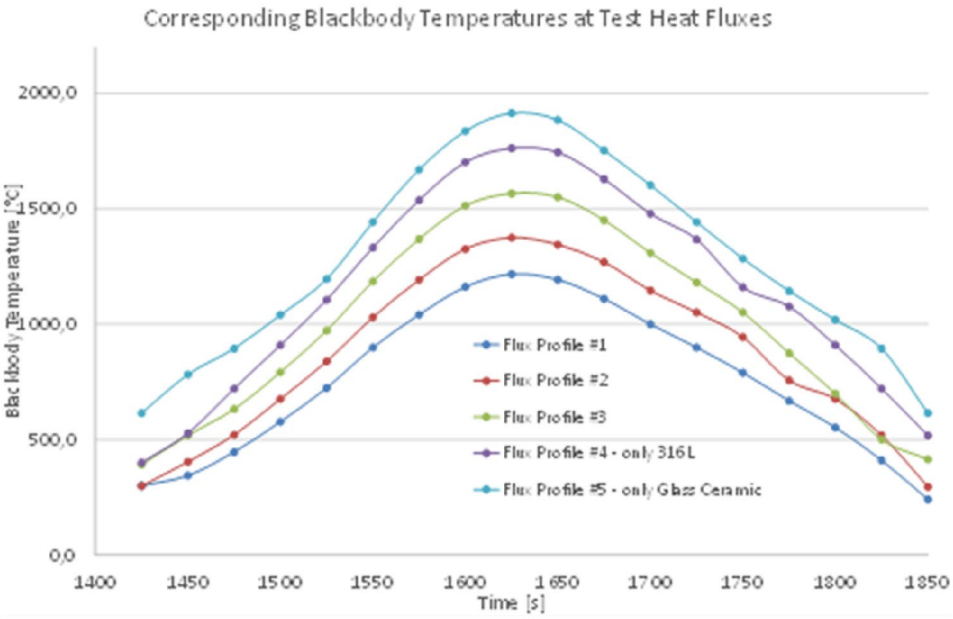

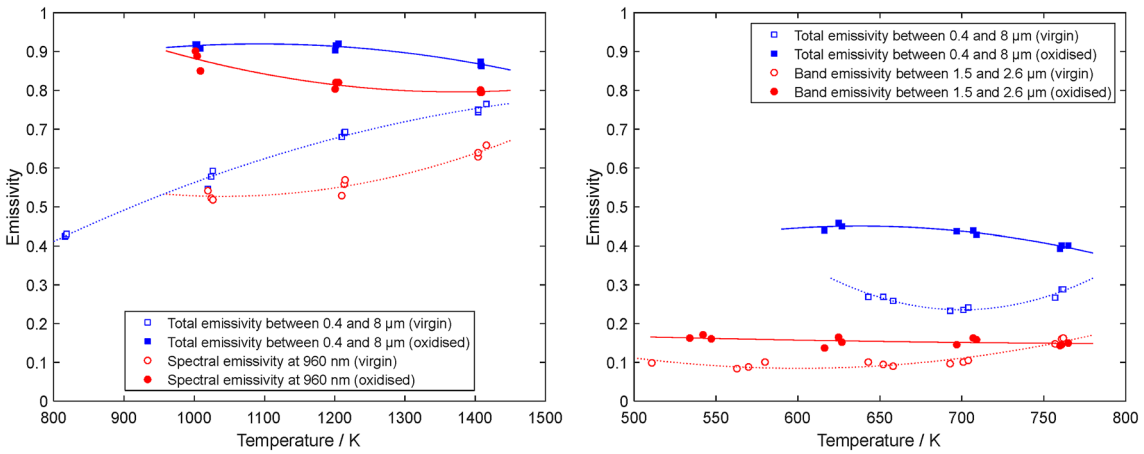

Fig. 6 Corresponding blackbody temperature for test heat fluxes

Fig. 7 Measured temperature-dependent total and device-specific emissivities of virgin and pre-exposed samples for aluminium alloy 7075 (left) and type 316L stainless steel (right)

expected for the tests at low heat flux and only slow oxidation at the higher heat flux condition. However, mechanical destruction due to thermal stresses was expected, but no cracking was observed and the samples showed a good resistance to thermal shocks throughout the testing. Please regard that mechanical properties of ceramics in general scatter significantly, highly depend on defect and geometry and require testing of a high number of specimens. The only four tests presented here do not prove that the material will generally survive such thermal shocks.

The colour of the samples changed during testing and it seemed that the surface was covered by a thin porous silicon dioxide layer. This layer had slowly grown over time after a sufficiently high temperature was reached. The exact effect of the silicon dioxide layer on the heat flux remains unclear, but it is assumed that a reduction in the sample temperature was caused by this layer. Except for this surface passivation, no demise could be observed during the low heat flux tests and, despite the higher temperatures due to the higher heat flux, no demisability could be observed at high heat flux either.

5.5 Plasma wind tunnel tests in the CoDM study

For air-plasma-exposed samples of aluminium alloy 7075, a rapid demise through melt was universally observed for each experiment, starting at low nominal heat fluxes as low as 125 kW/m^2, which was the lowest load applied during

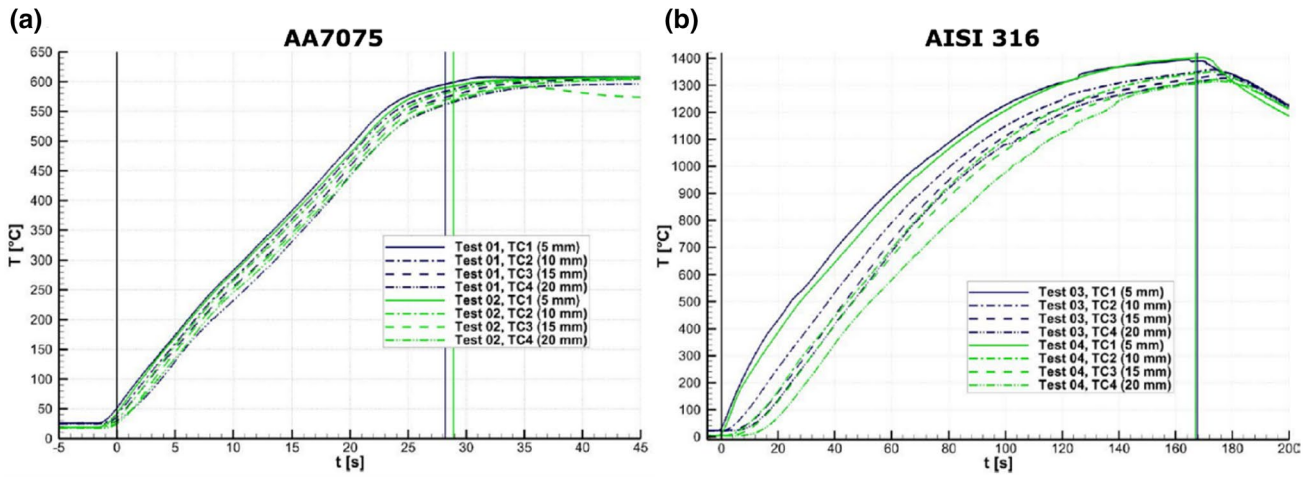

Fig. 8 Plasma wind tunnel tests of AA7075 and AISI 316

the CoDM PWT test campaign conducted at IRS. While it was generally found that the survivability duration of this and other aluminium-based alloys appears to roughly scale inversely with the applied heat flux, the actual demise often manifests itself in a comparatively sudden and rapid event. Rather than gradually shedding molten layers of material, the liquefied bulk would typically be retained for a significant amount of time within a barrier or "pouch" formed by a layer of surface oxides. This pouch would eventually tear under the influence of mechanical forces, e.g. gravity, discharging the liquid bulk in a singular event as depicted in Fig. 10.

Following the CoDM activity, subsequent tests at IRS have indicated that the melt-retaining and thus demise-delaying effect of oxide "pouches" is not universally relevant, with the material's demise phenomenology likely being sensitive to both aerothermodynamic heating conditions promoting varying degrees of oxide layer growth rates, as well as other influences such as external strain. With the later tests having been conducted using sample coins that were thinner than originally, with further minor modifications to the test setup resulting in an increased mechanical strain on the sample coins as applied by the spring-loaded fastening mechanism of the sample holder, these samples tended to succumb to softening and deformation in analogy to the phenomena reported from the CHARDEM campaign, while also clearly indicating the formation of a melt-retaining oxide layer.

Similar observations were made during the aluminium alloy plasma tests at VKI with complete demise of alloys Al2099 and Al7075 both at moderate (260 kW/m^2) and low heat fluxes (100 kW/m^2). However, the process to demise at low heat flux differed between the two alloys. While Al2099 formed an oxide layer at the surface, this layer cracked open after a certain time exposing the molten

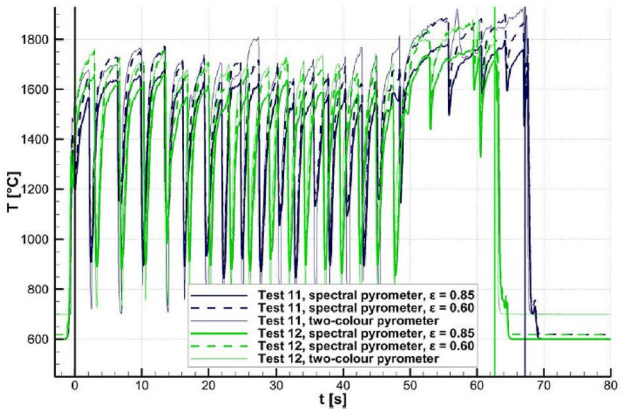

Fig. 9 Plasma wind tunnel test of CFRP—layer-by-layer ablation

aluminium core to the plasma flow. For the second alloy with Zinc as primary alloying element (Al7075), a thin layer of molten aluminium formed at the exposed surface without surface cracking.

Whereas no melt-retaining oxide pouch formation was observed for type 316L stainless steel, the singular test case that resulted in aerothermal demise at a fully catalytic heat flux of 920 kW/m^2 during the initial CoDM test campaign at IRS nonetheless resulted in a significant delay in the onset of demise through melt, which occurred only after 180 s (see also Fig. 11).

This is attributed largely to a thick oxide layer forming on its exposed surface, which appeared to serve as both a thermal as well as a limited mechanical barrier, delaying both the melting process as well as the physical loss of the comparatively viscous molten material, on top of considerably increasing the emissivity and thus the heat dissipation rate of the sample. As opposed to aluminium alloys, mass loss appears to occur in a generally more gradual fashion for

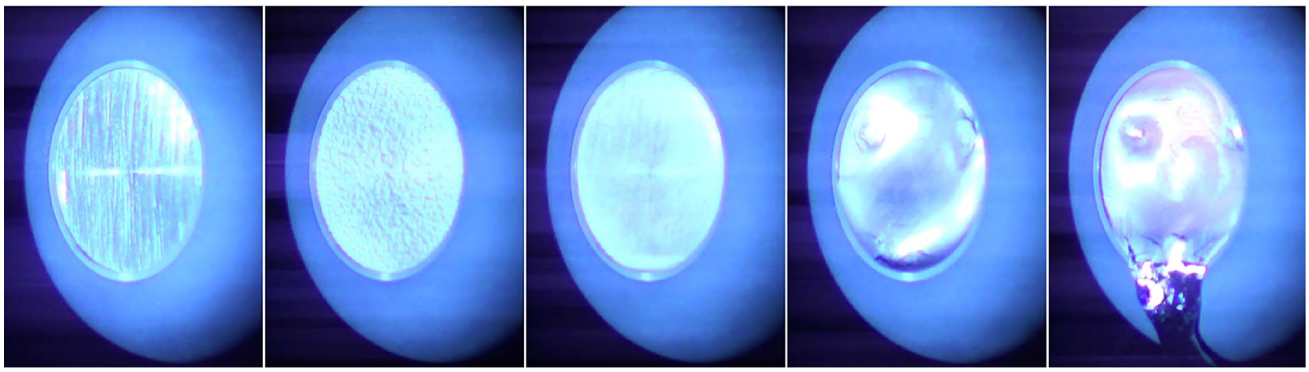

Fig. 10 From left to right: video stills of exposed surface of aluminium alloy 7075 sample #10 subjected to moderate heat flux condition at fully catalytic reference heat flux of 430 kW/m^2 and total pressure of 420 Pa

stainless steel, which is attributed to its comparatively lower thermal conductivity promoting a localised, gradually growing formation of molten pockets of material. Subsequent follow-up experiments conducted at significantly higher heating rates, have mostly been consistent in this observed phenomenology, albeit with the onset of mass loss generally occurring much sooner, i.e. within tens of seconds. The extreme delay observed in the early destructive CoDM test is attributed to the applied heating rate barely exceeding the presumed effective threshold required to effect demise, allowing the oxide layer and the sum of therewith connected demise-delaying effects to build up. For non-destructive test cases conducted at lower heat fluxes, the appearance and colouration of passive oxide layers formed on the surface of exposed type 316L stainless steel differed considerably between specimens subjected to different conditions, indicating that different (constant) air flow environments, respectively promote the formation of distinct oxide layer compositions.

The plasma tests at VKI at cold wall heat fluxes of 520 kW/m^2 and 260 kW/m^2 at 70 hPa total pressure support those observations. The steel coupon sample tested at 520 kW/m^2 started melting at the periphery after 28 s and the front surface after 42 s. During the transient heating phase (first 60 s) the surface colour varied from brown–red–blue to intense green, most likely due to the formation of different metal oxides. Accordingly, the emission signature showed atomic lines of Ni and Cr. The experiment at 260 kW/m^2 did not cause any melting of the steel coupon sample when a SiC cover was used. However, the same experiment was carried out with using a graphite cover, which showed signs of molten ring along the steel sample border after 50 s of plasma exposure. As a conclusion, this was later on attributed to carburization with the graphite holding cap. The sample back-wall temperature measured by thermocouples was 100 °C lower when using SiC cover instead of graphite.

With transient response test conditions effected during the CoDM test campaign being limited to a fully catalytic heat flux of less than 1.0 MW/m^2, none of the tests conducted on Ti-6Al-4V resulted in a demise of the respective specimen within a flight-representative duration of exposure. However, a variation in visually observable in-situ responses and post-test sample appearances was noted for Ti-6Al-4V samples exposed to distinct environmental conditions, i.e. differing total pressures, mass-specific enthalpies, accordingly resulting heat fluxes. In many cases, a persistent liquid oxide film, believed to consist primarily of vanadium(V)-oxide, was observed, which would re-solidify and in some cases be blown off due to thermomechanical shearing upon cool-down following the termination of experiment. This would reveal a surface modified by oxidation and/or alpha case formation to varying degrees. PWT experiments conducted during an IRS-internal follow-up to the CoDM activity at fully catalytic heat fluxes around 2.1 MW/m^2 have led to a demise behaviour consistent with that observed in the CHARDEM test campaign at DLR under comparable heat loads. Below such heating rates, the aforementioned liquid oxide film would appear to be actively decomposing under moderate heating rates around 1 MW/m^2, likely absorbing heat that would otherwise be available to liquefy bulk material.

In the case of CFRP EX-1515/M55J, only isolated delamination events were observed during the test conducted at IRS. While the lateral mechanical constriction of the sample has been noted to largely suppress post-char delamination, this particular material maintained cohesion even after extraction, indicating that the char residue maintains strong binding properties for relevant timeframes. This resulted in mass loss occurring almost exclusively due to pyrolytic decomposition and surface ablation through active oxidation of the exposed, pre-charred material. In accordingly measured temperature histories, as shown by example in Fig. 12, this is reflected by a gradual and nearly uniform convergence

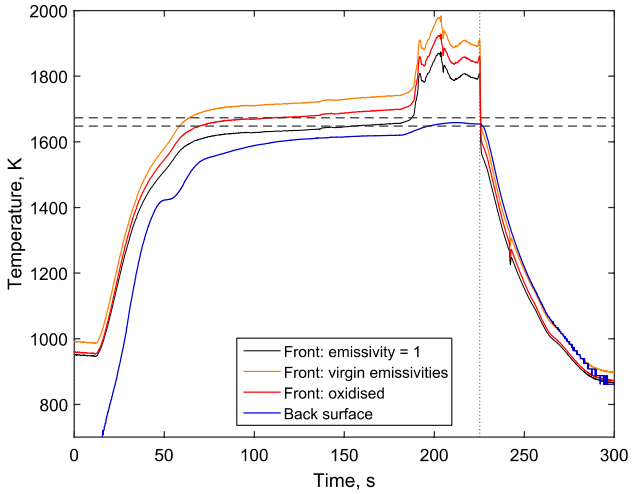

Fig. 11 Plasma wind tunnel test results for pyrometrically measured surface temperature history for type 316L stainless steel with mechanical constriction of sample indicating gradual ablation. Depicted results represent CoDM sample AISI 316L #10 subjected to high heat flux condition at fully catalytic reference heat flux of 920 kW/m^2 and total pressure of 19 hPa

of the front and back surface temperature curves, with few initial minor delamination events occurring during the first 3 min of testing being reflected through temperature jumps.

None of the transient PWT experiments conducted on SiC samples during the CoDM test campaign resulted in aerothermal demise or thermomechanical shattering. However, each sample formed a passive oxide layer, the net thermodynamic effects of which appear to be subtle at best. These would specifically result from alterations in the thermo-optical and aerothermochemical, i.e. catalytic, properties of the surface, as evidenced both by the pre- and post-test characterization of the material's total emissivity as well as by the highly regular and consistent nature of the recorded surface temperature histories. These reflect a complete lack of phase changes or other thermodynamically relevant processes occurring within the bulk of the heated material. Due to this consistency and reproducibility, SiC is considered an excellent benchmark against which to interpret the thermal response of other materials subjected to identical aerothermodynamic heating conditions.

For all of the materials investigated in CoDM, temporally resolved boundary layer spectra were measured in intervals. Atomic and diatomic species emanating from the exposed material surfaces into the boundary layer were identified and correlated with different material states and plasma-wall interaction phenomena. An according first assessment of these spectra was provided in Ref. [19] and will be elaborated upon further in future publications.

5.6 Post-test characterization (CHARDEM)

Figure 13 shows photographs of the metal samples before and after plasma wind tunnel testing as well as their microstructure. Various degrees of demise and surface degradation were observed.

The AA7075 sample (Fig. 13a–c) shows overheating above the solidus of the entire specimen resulting in softening and deformation of the material due to melting or partial melting. Under the loads of the plasma-jet, the softened front-side-material was transported from the front towards the back-side of the specimen while being wrapped in an oxide pocket (Fig. 13c). The oxide skin appears to be quite stable, covering the entire specimen and protecting the molten or partially molten material from being blown away. This was also confirmed by the observations during the PWT experiments, according to which there was no mass loss of the specimen. The hardness of the material decreased from approximately 180 HV down to a level of 110–140 HV as a direct consequence of the heating.

The AISI 316 sample shown in Fig. 13d–f mainly kept its geometry. It can be observed, that there is no or little impact on the geometry except for a few areas where droplets have formed on the edges, indicating that some melting took place. The front surface is still existent, but it has clearly degraded and crater-like structures and blisters are existent (Fig. 13e). SEM–EDS analysis confirmed that the entire surface exposed during the PWT test is covered with an oxide layer (Cr-rich). It is believed that due to local break-up of the oxide layer the molten surface material was spilled in small, drop-like portions. In addition, the inner structure of the AISI 316L showed signs of overheating, creating shrinkage porosity near the surface and the hardness was clearly reduced post-PWT testing (Fig. 13f).

The Ti-6Al-4 V sample, shown in Fig. 13g–i, exhibits an oxide layer at the front surface, which appears to have broken away locally and was replaced by a new oxide layer (Fig. 13h). Underneath the oxide, a brittle alpha case microstructure formed, supported by O and N, diffusing into the surface-near zone at elevated temperatures (Fig. 13i). The microstructure exhibits grain coarsening underneath the front surface. The hardness was measured to be similar to the pre-test material, except for the alpha-case regions, where the hardness increased and the material became brittle. At the front side at the edges of the sample, the material appears to have molten. The melting is thought to have been supported by the comparably low thermal conductivity resulting in an overheating of the surface at the exposed edges.

The microstructure of an additively manufactured (AM) Ti-6Al-4V samples post-PWT testing was examined as well. Additive manufacturing is a process that is increasingly popular in the space industry due to its potential for weight and cost savings as well as additional functionality.

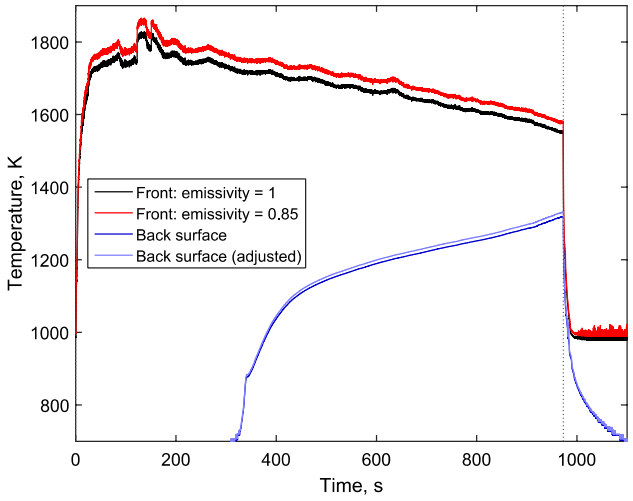

Fig. 12 Plasma wind tunnel test results for pyrometrically measured surface temperature history for CFRP with mechanical constriction of sample indicating gradual ablation. Depicted results represent CoDM sample CFRP EX-1515/M55J #08 with initial thickness of 4.06 mm subjected to Moderate Heat Flux condition at fully catalytic reference heat flux of 430 kW/m^2 and total pressure of 420 Pa

Despite slight differences in the virgin microstructure (AM samples exhibit melt tracks for instance), the effects of the PWT testing on the samples seem to be very similar to the conventional Ti-6Al-4V samples, as shown in Fig. 14.

Figure 15a shows a CFRP sample before testing with the fibre layers all tightly packed into the thermosetting polymer matrix. In contrast, Fig. 15b shows the same CFRP sample after PWT testing, which exhibits significant degradation. It can be observed, that the matrix polymer on the front side has vanished, with only the carbon fibres remaining in loose form. A result of this is a reduced sample thickness caused by delamination and blow-off of the fibre layers during the test. According to FTIR, the matrix polymer on the CFRP samples is epoxide.

Figure 15c exemplarily shows that the SiC samples did not exhibit geometrical changes after testing. Merely, discoloration of the exposed surface hints at the growth of a surface layer during testing. SEM–EDS analysis of the surface confirmed the existence of a surface layer with the main constituents being Si and O. The bulk of the SiC sample was observed to be unchanged from its virgin state.

6 Numerical rebuilding of the demise tests

In the CHARDEM study, the demise tests and the mass loss experienced by the samples during PWT testing were calculated via the SCARAB software and compared to the measured test results. For the aluminium and titanium alloys, the mass loss experienced was found to be significantly lower than that calculated with SCARAB using the original material properties. For instance, the total measured mass loss of the Ti-6Al-4V sample was on average 1.1 g (initial mass 171.5 g) and was calculated as ~ 5 g by the software. It was concluded that SCARAB was too optimistic on the demise of these materials (e.g. simulated melting event occurring earlier than in reality) mainly because of the values for the material properties being used. In contrast, for the CFRP samples, the mass loss was considerably underestimated because of the unexpected layer-by-layer ablation process of that material, that is typically not observed for CFRP. Here, the actual mass loss was ~ 40 g, whereas the calculations yielded only about 7 g. This clearly shows the need to investigate the demise process and behaviour of every material being considered. For the other materials analysed in this study, the measured data compared better with the simulations, although some differences were still identified. The discrepancies uncovered in this study show the need for more accurate data to be fed into and models to be used by the simulation tools.

This is also true for the prediction of the time versus temperature plots simulated in SCARAB, as shown in Fig. 16 for AA7075. Each line in the plot corresponds to a temperature measurement at a certain depth in the sample, either measured (L2K) or simulated (SCARAB). It can be observed that the lines in the plot form two groups. The measured (L2K) data forms one group where the peak temperatures are achieved later. This results in a later melting of up to 10 s compared to the second group, which is formed by the simulated (SCARAB) data. Please regard that this means an overestimation of the heating rate by approx. 22%. This is mainly induced by the incorrect material properties, but other uncertainties all play a role (e.g. the uncertainty in the heat flux calibration in the wind tunnel or the primitive model used for calculation of the heat flux distribution used by the old SCARAB version).

After exchanging the original material data in SCARAB in favour of the data measured in the project, the discrepancy could be reduced significantly. Figure 17 shows this improvement of the numerical rebuilding. Comparison of the thermophysical data showed, that the original heat capacity values were wrong.

The data of the other metals and SiC shows reasonable correspondence with the simulated results, while the CFRP data again shows significant discrepancies due to the layer-wise degradation, which could not be simulated by the software. The need for more advanced modelling approaches is apparent and is currently being addressed in ongoing projects.

Rather than using a single test to demise the material, the CODM study ran a series of tests at different heat flux levels. This allowed assessment of steady state heat balances,

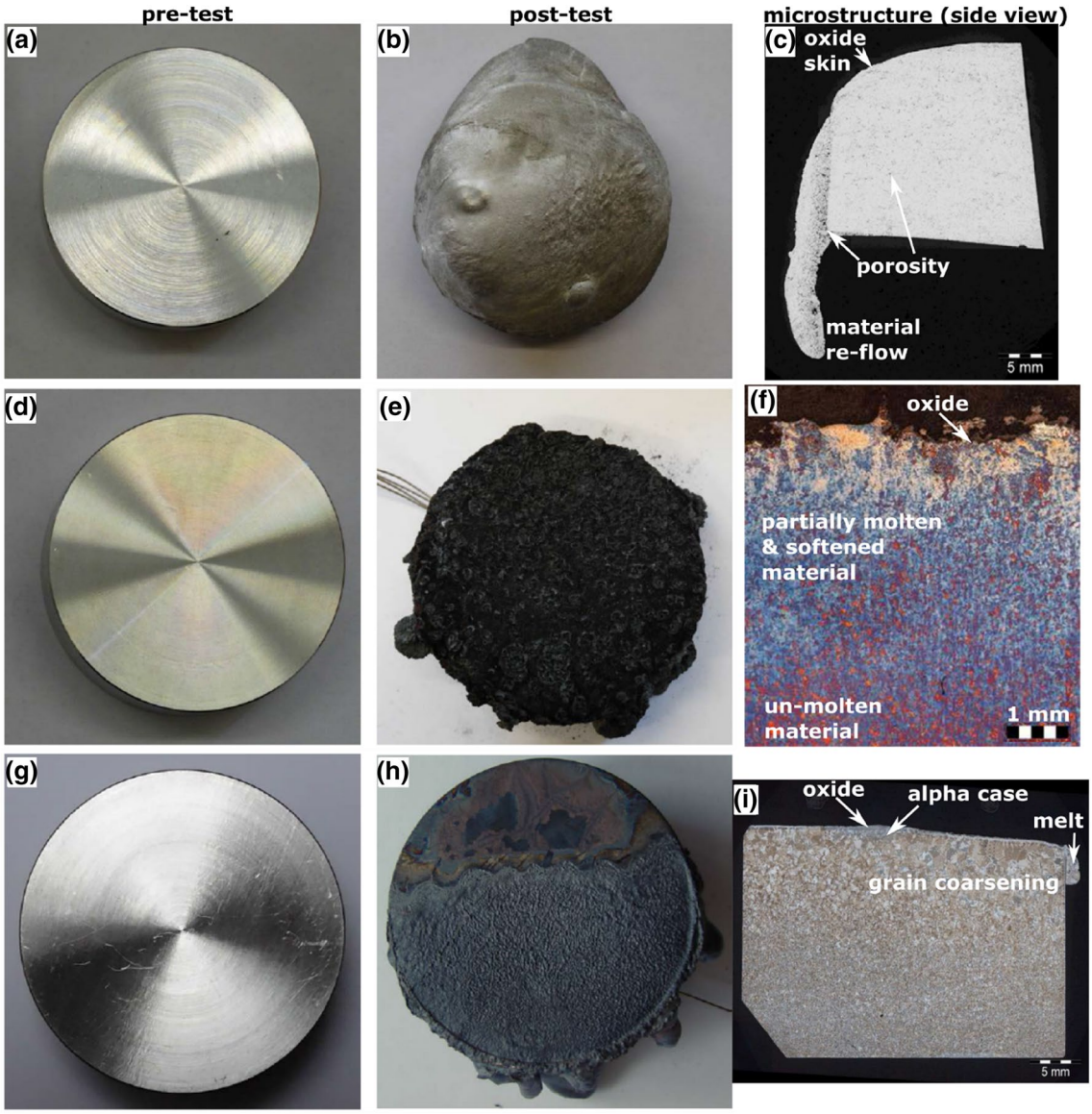

Fig. 13 Photographs before/after wind tunnel experiments (AA7075 top, AISI316L middle, Ti6Al4V bottom). First column: untested samples; second column: tested samples; third column: microstructure after the testing

which allowed an understanding of the material emissivity, which was also measured, and the material catalycity to be assessed. The sensitivity of the steady state surface temperatures to the models is clearly demonstrated in Fig. 18 for the stainless steel A316L material. The original model results in an overprediction of the steady state temperature by 120 K. Using the measured emissivity value, which is higher than in the previous models, improved the prediction error to 40 K. Use of a catalycity model for stainless steel results in a 10% reduction in the incoming heat flux and a very good agreement with the measured steady state temperature.

Similar, but more extreme observations were made for the titanium Ti6Al4V material, with the initial errors in the steady state temperatures being of the order of 400 K and the reduction in heating due to the catalycity being 20% in that case. This highlights the value of performing steady state heating tests as the heat balances are very sensitive. Being able to capture the steady state temperatures provides significant confidence in the wind tunnel conditions and material models which cannot be obtained as easily by a rebuild of the transient data.

The transient data was also rebuilt using SAMj, with an example of the rebuild of the titanium material shown in Fig. 19. Again, the surface temperatures are shown (Fig. 20).

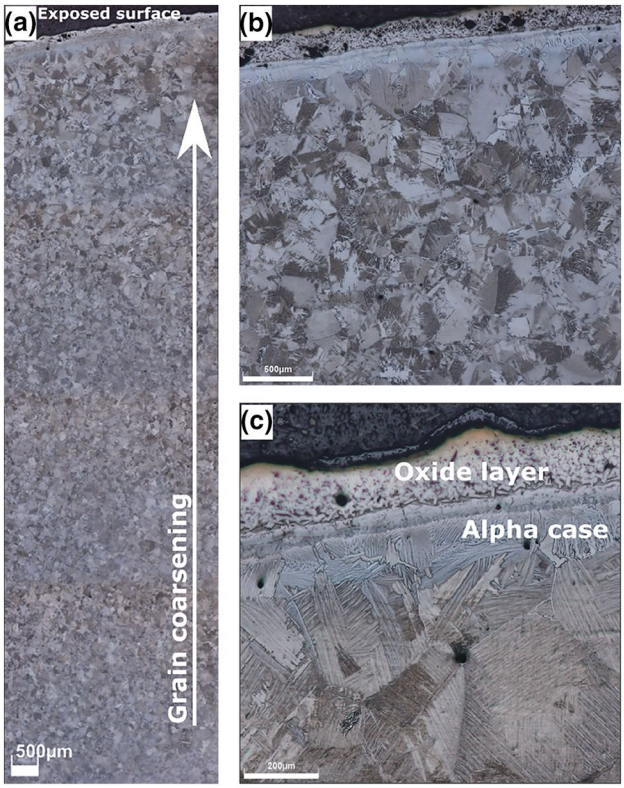

Fig. 14 Additively manufactured (AM) Ti-6Al-4V microstructure after PWT testing

For the AA7075 aluminium alloy, tests were performed in IRS and in the VKI Plasmatron. The material is sufficiently high conductivity to be essentially isothermal in this case, and the temperature is given by a back face thermocouple. As aluminium is such a low melt temperature material, no steady state testing was possible. The SESAM material model is approximately equivalent to the SCARAB model used in the CHARDEM rebuilds above, but the SAMj model, which was based on NIST-JANAF data for pure aluminium performs very well. It is interesting to note that there was no predicted reduction in the heat flux due to catalycity, and that the melt of the aluminium alloy occurred between the values in the SAMj and SESAM models. More recent modelling has resulted in the models adopting an intermediate value of 850 K for the effective melt temperature in both tools [20].

The work on the emissivity and catalycity values in CoDM has driven recommendations that unknown emissivity values should consider high numbers, such as 0.8, and this has been adopted into the ESA demise verification guidelines (DIVE). This has confirmed other researchers findings [21] that oxidized emissivities, and not virgin emissivities, should be used re-entry studies. Following the demonstration of its value, a similar catalycity model to the one developed in SAMj has been implemented into ESA's DRAMA tool.

7 Summary and discussion

At the beginning of this publication, it was argued that demisability should become an additional material property to be considered during the material selection process for future space missions. This requires a solid basis of demise-related material data. Therefore, demisability test procedures were developed starting with the measurement of thermophysical properties, followed by plasma wind tunnel (PWT) testing and post-test characterization of the material. The testing methodologies developed during the two activities were then later used as baseline for writing the DIVE document (Guidelines for Analysing and Testing the Demise of Man Made Space Objects During Re-entry). The methodology is used in characterisation of new materials, not yet present in the re-entry software database. Finally, the measured data was compared to the results from computer simulations performed with the SCARAB and SAM software. Three metallic materials, one ceramic and one composite (CFRP) that are commonly used for space applications were analysed in this study.

The thermo-physical properties are very important for the prediction of the demise behaviour. High-quality data was acquired for the metallic samples (AA7075, AISI 316 and Ti-6Al-4V) up to their respective melting points. Due to the high decomposition temperature of SiC, the properties of this material were measured up to maximum possible of 1500 °C. The CFRP samples structurally disintegrated at elevated temperatures. Therefore, some thermophysical properties could be measured only in a lower temperature range. This caused some problems with the simulations as accurate material data are necessary for obvious reasons.

The thermo-optical and thermo-chemical properties, i.e. specifically the emissivity and catalytic behaviour of the respective materials are further critical in predicting demise, as these effects determine the surface energy balance of an object undergoing re-entry heating. This accordingly determines the amount of absorbed heat that becomes available to drive the various material-characteristic decomposition processes in the first place. Emissivities of the primary candidate materials were characterised for temperatures ranging up to near the respective critical demise-relevant temperatures for both virgin materials and such previously subjected to near-destructive plasma wind tunnel testing under entry-relevant conditions. Steady-state thermal response measurements under air plasma heating conditions, yielding relevant equilibrium temperatures for the investigated high-temperature materials titanium, stainless steel and SiC, were further conducted to provide a baseline for assessing

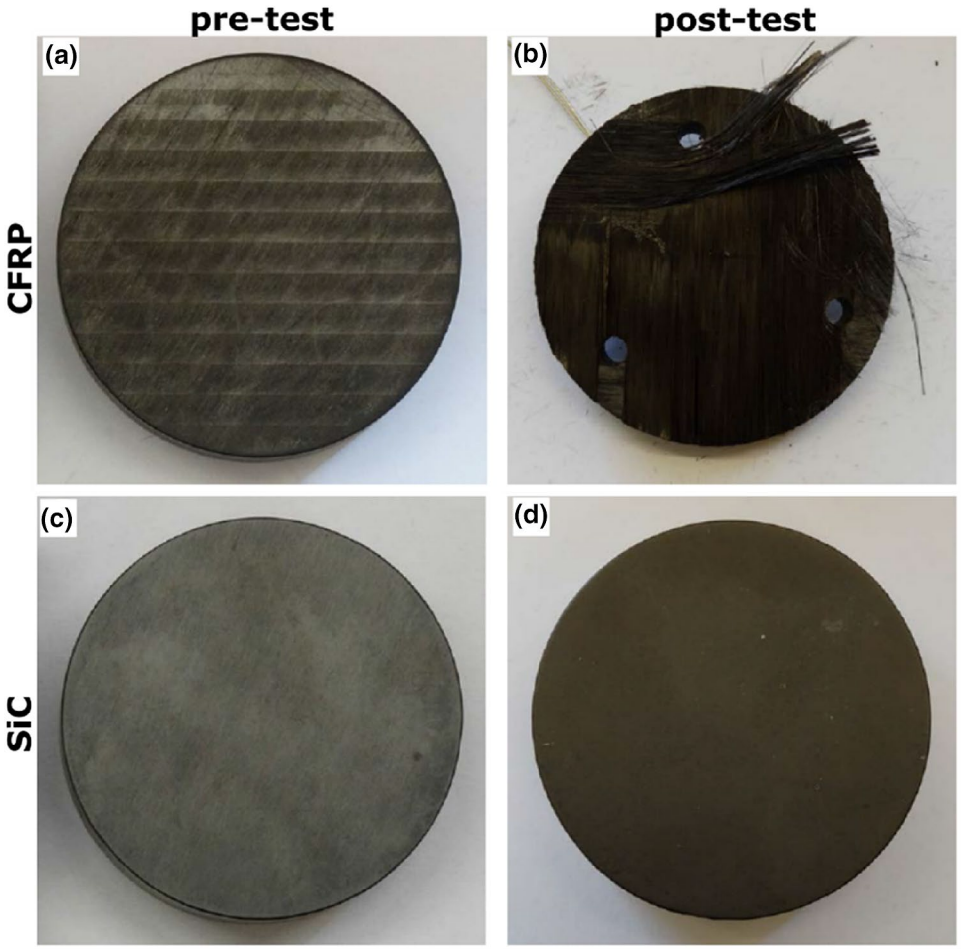

Fig. 15 Photographs of the test samples: CFRP (**a, b**) and SiC (**c, d**) before (**a, c**) and after (**b, d**) the tests

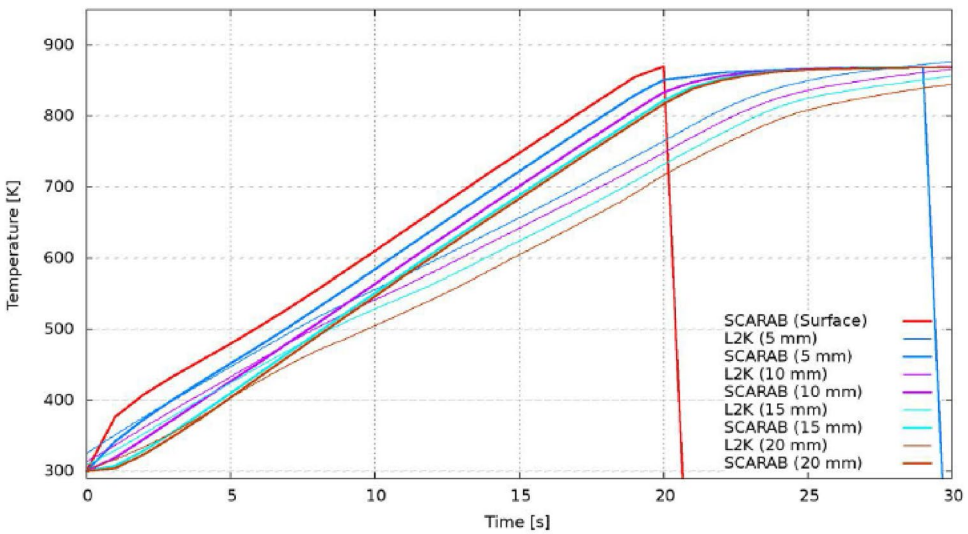

Fig. 16 Time versus temperature plot of AA7075: comparison of measured (L2K) data with simulated SCARAB data at different depths in the sample

the relative thermodynamic effects of catalytic recombination at the exposed surface for these materials.

Transient, i.e. destructive PWT testing showed some very interesting results and highlighted that for some materials the demise processes are not fully understood yet. In some test cases, the aluminium alloy began deforming before reaching its melting point, but was contained in an oxide

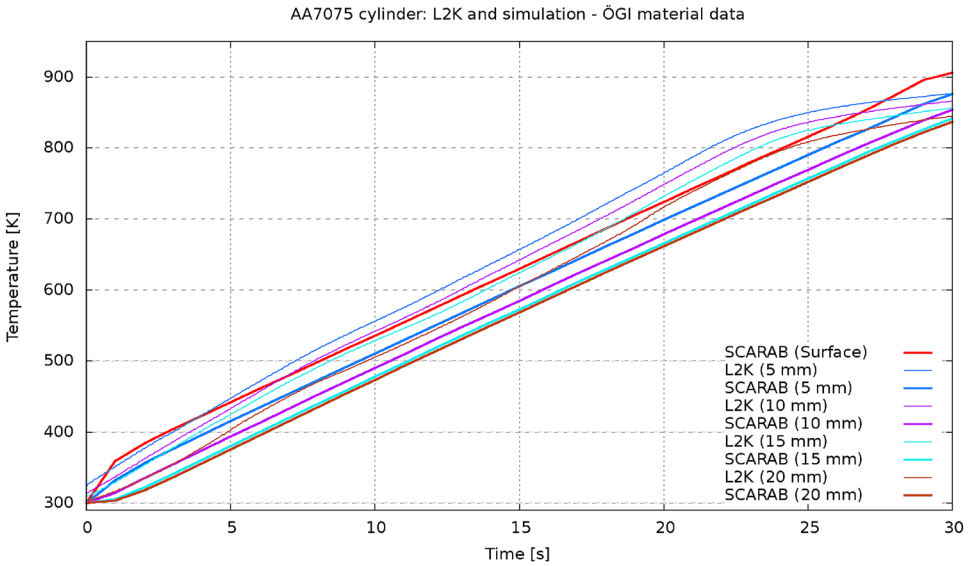

Fig. 17 Time versus temperature plot of AA7075: comparison of measured (L2K) data with simulation using measured thermophysical data as inputs at different depths in the sample

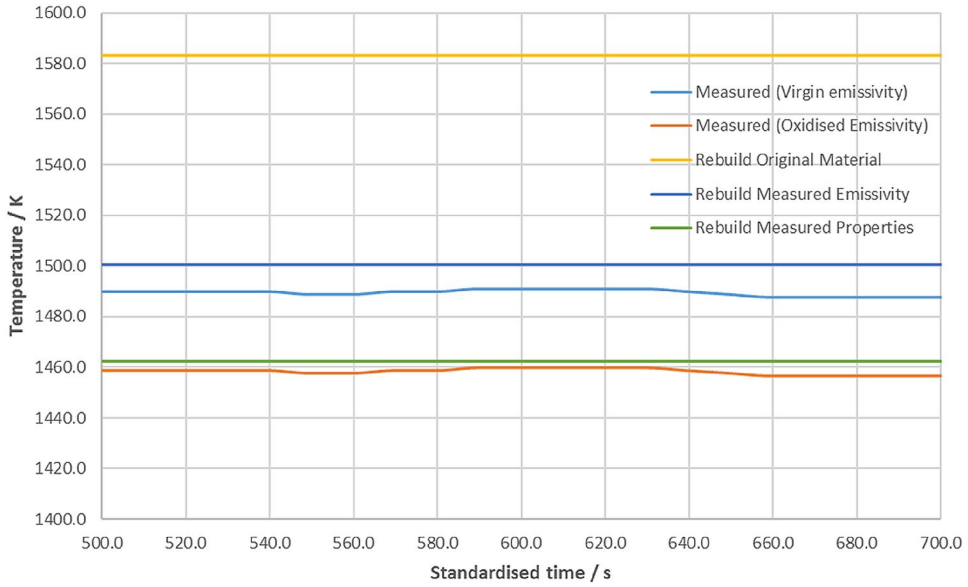

Fig. 18 Steady state portion of low flux steel test

bag that prevented the spillage of the material. It is unclear, which impact this has on the demise of a satellite during the real entry flight. An oxide layer was also discovered on the PWT tested stainless steel samples. This surface layer was found to be dark in the visual and infrared range, therefore raising the thermal emissivity of the material during the test. This effectively reduced the demisability of the material due to the radiation of absorbed heat. A similar observation was made for Ti-6Al-4V, which in addition to high emissivity also has a high melting point. The growth and occasional detachment of the oxide layer observed on the titanium samples under the lower heat-flux conditions in CHARDEM further decreased the heat flux and partially insulated the solid material behind the oxide layer. This led to very low demisability. Demise was observed only at very high heat loads (typical for eccentric re-entry flight), which is a very important result. The CoDM test results showed deviating findings concerning the qualitative demise behaviour of Ti-6Al-4V. Whereas quantitative findings overlap between both test campaigns in that no demise was observed at heating rates below 2 MW/m^2, such samples subjected to moderately high heating rates formed a liquid oxide film. Spectroscopic evidence indicated that this was likely dominated by vanadium(V)-oxide, which appeared to be actively "boiling", i.e. decomposing at temperatures slightly exceeding the liquidus of the alloy. With this decomposition of vanadia being endothermic, it is believed that this effect

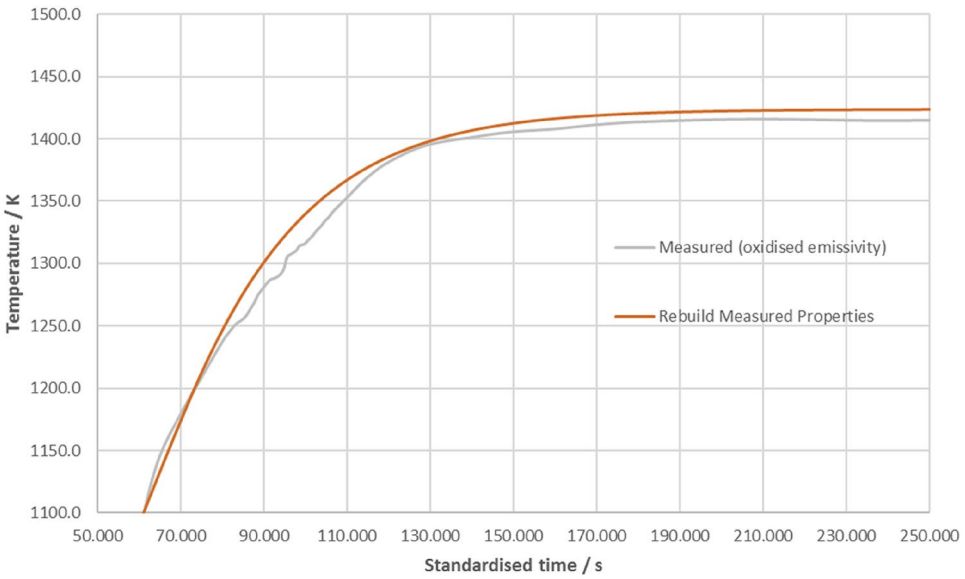

Fig. 19 Rebuild of titanium heat-up using SAMj with updated emissivity and catalycity models

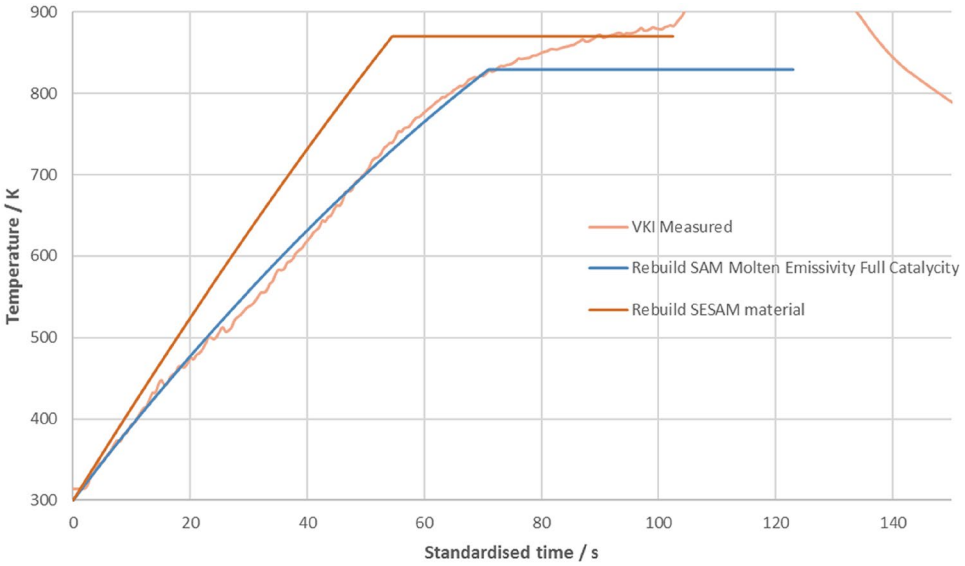

Fig. 20 Rebuild of aluminium heat-up and melt using SAMj

may contribute to a delayed demise in an effectively similar albeit more constant manner as compared to the periodic macroscopic shedding of solid oxide layers reported in the CHARDEM study. Aluminium could also be one constituent element of the alloy actively boiling behind the oxide layer in a low pressure environment. Further research is required on this topic.

Ti-6Al-4V is increasingly used on spacecraft due to its low mass and excellent mechanical properties. The data on its demise-characteristics will be used in the design and material selection of future missions. As the heat flux is of great importance, considerations regarding the position of Ti-6Al-4V within the spacecraft/satellite, total mass and geometric shape will have to be made. Furthermore, as additively manufactured (AM) Ti-6Al-4V parts and components are quickly gaining prominence in new spacecraft design, their demise properties have to be established as well. Therefore, the CHARDEM study included PWT testing of an AM Ti-6Al-4V sample, with almost perfectly identical results to the conventional Ti-6Al-4V. Although no major differences between the two were expected, the AM Ti-6Al-4V does exhibit slightly different microstructure and surface roughness. However, these did not seem to have a relevant impact under the test conditions.

The Ti-6Al-4V material has also been demonstrated to have a relatively low catalycity in the CoDM study, with the incoming flux being reduced by approximately 20% relative to a fully catalytic value. This further reduces the demisability of this material.

This study showed no demise of the SiC and unexpected behaviour of the CFRP, supporting the argument that more data is needed to understand their demise processes. The tested SiC showed no demisability at low or high heat inputs, probably a result of its very high decomposition temperature and the growth of a protective oxide skin. The expected brittle behaviour or cracking induced by the high thermo-mechanical stresses were not observed. The catalycity of SiC was the lowest of the materials tested in CoDM, with heat flux reductions of the order of 30% observed.

The CFRP samples showed surprisingly high demisability in the CHARDEM study. This is with reference to previous observations such as the CFRP tank from the Atlas Centaur upper stage that survived atmospheric re-entry. The decomposition of the matrix and periodic mechanical ablation of the fibre layers appeared to be responsible for the fast demise of the CFRP samples in this study. On the other hand, the variant of CFRP tested in the CoDM test campaign saw very little delamination, owing in part to the lateral constriction of the sample but primarily to the strong bonding power of the char residue. This resulted in low mass ablation rates reminiscent of the behaviour of ablative TPS materials. Other test campaigns that are not shown in this paper indicate, that the geometry and the composition of the matrix may be a very important factor. Further testing in this area is clearly needed and has been or is being addressed since the project summarised in this paper [22].

Finally, numerical simulations showed that there are already software tools available that can model the demise of some materials with acceptable accuracy. However, the results of these simulations have shown to depend on the quality of the data that was put in. While standard material data showed rather large discrepancies between real demise and the simulations, input of the measured thermo-physical data achieved much more accurate results. The steady state temperature data, which is highly sensitive for the simulations to capture demonstrate that the emissivity and catalycity are critical parameters for high temperature materials. Aluminium is slightly different in that it has a lower melt temperature, and the melt temperature is more critical. Errors in the aluminium models seen are in the specific heat capacity, but this was an error specific to particular tools.

8 Conclusion

The two activities CHARDEM and CoDM allowed to understand better the demise behaviour of five materials often used on LEO missions. The behaviour of metallic materials in the harsh entry environment is not fully understood and the numerical modelling, which uses several different simplifications, shows relevant disagreement between the tests and the numerical rebuilding. However, these discrepancies are deemed acceptable and the performed numerical simulations are considered representative of the results obtained in experimental simulations. The exact phenomenology and thus the degree to which certain models reflect the actual behaviour of the metals is assumed to depend on the specifics of the environmental heating conditions, as exemplified by the variety of post-test phenomenologies observed for metal alloys. The relevance of certain secondary effects such as the formation of oxide pouches and the retention of molten bulk material delaying mass loss, were only observed in some test cases.

Characterisation of thermo-physical properties up to the melting/decomposition range of the materials must be considered, as it is essential for decreasing the uncertainty associated to material demise during re-entry simulation. The main outcome regarding metallic material testing was the increased emissivity measured in the oxidised conditions at high temperatures. High emissivity values can cause a steady state condition for high melting points metals even at high incident heat flux rates. Re-entry software previously considered virgin thermal emissivity of 0.3 or even less for metallic materials (e.g. 0.05 for aluminium in SCARAB), while total emissivity in oxidised condition was measured to be in the range of 0.7–0.9.

Composite demise is not understood and many aspects, such as resin and fiber types, fiber volume fraction, manufacturing process and others, that impact the demisability, should be studied further. To mitigate this lack of understanding, the demise behaviour of composites and the influence of respective relevant material parameters is currently being investigated within the ongoing follow-up study COMP2DEM.

All the work performed during this activity helps decreasing the uncertainties associated to material modelling during uncontrolled atmospheric re-entry events. The material data generated can directly be used by the re-entry software for casualty risk assessment at satellite level or for design for demise at equipment level.

References

1. Kuiper, W., Drolshagen, G., Noomen, R.: Micro-meteoroids and space debris impact risk assessment for the ConeXpress satellite using ESABASE2/Debris. Adv. Space Res. **45**, 683–689 (2010). https://doi.org/10.1016/j.asr.2009.10.020
2. Grassi, L., Tiboldo, F., Destefanis, R., Donath, T., Winterboer, A., Evans, L., Janovsky, R., Kempf, S., Rudolph, M., Schäfer, F., Gelhaus, J.: Satellite vulnerability to space debris—an improved 3D risk assessment methodology. Acta Astronaut. **99**, 283–291 (2014). https://doi.org/10.1016/j.actaastro.2014.02.006
3. Kelley, R.L.: Using the design for demise philosophy to reduce casualty risk due to reentering spacecraft. In: 63rd International Astronautical Congress (2012)

4. Waswa, P.M.B., Elliot, M., Hoffman, J.A.: Spacecraft design-for-demise implementation strategy & decision-making methodology for low earth orbit missions. Adv. Space Res. **51**, 1627–1637 (2013). https://doi.org/10.1016/j.asr.2012.11.020
5. Trisolini, M., Lewis, H.G., Colombo, C.: Survivability and demise criteria for sustainable spacecraft design. In: Proceedings of International Astronautical Congress IAC, pp. 2505–2523 (2015)
6. Trisolini, M., Lewis, H.G., Colombo, C.: Spacecraft design optimisation for demise and survivability. Aerosp. Sci. Technol. **77**, 638–657 (2018). https://doi.org/10.1016/J.AST.2018.04.006
7. Heinrich, S., Martin, J., Pouzin, J.: Satellite design for demise thermal characterisation in early re-entry for dismantlement mechanisms. Acta Astronaut. (2018). https://doi.org/10.1016/J.ACTAASTRO.2018.03.021
8. Lips, T., Fritsche, B., Kanzler, R., Schleutker, T., Gülhan, A., Bonvoisin, B., Soares, T., Sinnema, G.: About the demisability of propellant tanks during atmospheric re-entry from LEO. J. Space Saf. Eng. **4**, 99–104 (2017). https://doi.org/10.1016/J.JSSE.2017.07.004
9. Koppenwallner, G., Fritsche, B., Lips, T., Klinkrad, H.: Scarab-a multi-disciplinary code for destruction analysis of space-craft during re-entry. In: Fifth European Symposium on Aerothermodynamics for Space Vehicles, p. 281 (2005)
10. Lips, T., Fritsche, B.: A comparison of commonly used re-entry analysis tools. Acta Astronaut. **57**, 312–323 (2005). https://doi.org/10.1016/j.actaastro.2005.03.010
11. Lips, T., et al.: Re-entry risk assessment for launchers—development of the new SCARAB3.1L. In: Proceedings of the 2nd IAASS Conference "Space Safety in a Global World" Chicago, USA, ESA SP-645 (2007)
12. Lemmens, S., Funke, Q., Krag, H.: On-ground casualty risk reduction by structural design for demise. Adv. Space Res. **55**, 2592–2606 (2015). https://doi.org/10.1016/J.ASR.2015.02.017
13. Schüßler, M., Auweter-Kurtz, M., Herdrich, G., Lein, S.: Surface characterization of metallic and ceramic TPS-materials for reusable space vehicles. Acta Astronaut. **65**, 676–686 (2009)
14. Pagan, A.S., Massuti-Ballester, B., Herdrich, G.H., Merrifield, J.A., Beck, J.C., Liedtke, V., Stelzer, N., Bonvoisin, B.: Characterisation of demisable materials through plasma wind tunnel testing. In: 8th European Symposium on Aerothermodynamics Space Vehicles, Lisbon, Portugal (2015)
15. Herdrich, G., Fertig, M., Löhle, S.: Experimental simulation of high enthalpy planetary entries. Open Plasma Phys. J. **2**(1), 150–164 (2009). https://doi.org/10.2174/1876534300902010150
16. Bottin, B., Chazot, O., Carbonaro, M., van der Haegen, V., Paris, S.: The VKI plasmatron characteristics and performance. In: RTO AVT Course on Measurement Techniques for High Enthalpy and Plasma Flows, RTO EN-8, Rhode-Saint-Gebnese, Belgium, October 1999, pp. 6-01–6-26
17. Fagnani, A., Helber, B., Chazot, O.: Evaluation of probe-material thermal interaction in plasma wind tunnel tests by means of IR thermography and thermal inverse modelling. In: 8th European Conference for Aeronautics and Aerospace Sciences (EUCASS). https://doi.org/10.13009/EUCASS2019-413
18. Pagan, A.S., Massuti-Ballester, B., Herdrich, G.: Total and spectral emissivities of demising aerospace materials. Front. Appl. Plasma Technol. **8**(1), 7–12 (2016)
19. Pagan, A.S., Massuti-Ballester, B., Herdrich, G., Merrifield, J.A., Beck, J.C., Liedtke, V., Bonvoisin, B.: Investigation of the surface and boundary layer composition for demising aerospace materials. In: 7th International Workshop on Radiation of High Temperature Gases in Atmospheric Entry, Stuttgart, Germany (2016)
20. Holbrough, I., Beck, J., Braun, V., Lemmens, S.: MADRE: upgrading the re-entry risk component of ESA's DRAMA software. In: 8th European Conference on Space Debris, Online (2021)
21. Balat-Pichelin, M., Annaloro, J., Barka, L., Sans, J.L.: Behavior of TA6V alloy at high temperature in air plasma conditions: part 2—thermal diffusivity and emissivity. J. Mater. Eng. Perform. **29**, 4606–4616 (2020)
22. Beck, J., Holbrough, I., Schleutker, T., Guelhan, A.: Improved representation of destructive spacecraft re-entry from analysis of high enthalpy wind tunnel tests of spacecraft equipment. Acta Astronaut. **164**, 287–296 (2019)

Publisher's Note Springer Nature remains neutral with regard to jurisdictional claims in published maps and institutional affiliations.